Geochemistry, Geophysics, Geosystems®

AGU ADVANCING EARTH AND SPACE SCIENCE

RESEARCH ARTICLE
10.1029/2022GC010520

Hydrogen Diffusion in Clinopyroxene at Low Temperatures (195°C–400°C) and Consequences for Subsurface Processes

Thilo Bissbort[1,2], Kendra J. Lynn[3,4], Hans-Werner Becker[2], and Sumit Chakraborty[1,2]

[1]Institute for Geology, Mineralogy and Geophysics, Ruhr-University Bochum, Bochum, Germany, [2]Central Unit for Ionbeams and Radionuclides RUBION, Ruhr-University Bochum, Bochum, Germany, [3]Now at Hawaiian Volcano Observatory, United States Geological Survey, Hilo, HI, USA, [4]Department of Earth Sciences, University of Delaware, Newark, DE, USA

Key Points:

- Diffusion rates of hydrogen in clinopyroxene in the low temperature range (195°C–400°C) were quantified for the first time
- Diffusion coefficients at low temperatures lie within the range of extrapolations from high temperature experiments
- Non-isothermal modeling was applied to evaluate potential re-equilibration of clinopyroxene crystals at low temperatures

Supporting Information:

Supporting Information may be found in the online version of this article.

Correspondence to:

T. Bissbort,
thilo.bissbort@rub.de

Citation:

Bissbort, T., Lynn, K. J., Becker, H.-W., & Chakraborty, S. (2022). Hydrogen diffusion in clinopyroxene at low temperatures (195°C–400°C) and consequences for subsurface processes. *Geochemistry, Geophysics, Geosystems*, *23*, e2022GC010520. https://doi.org/10.1029/2022GC010520

Received 24 MAY 2022
Accepted 8 NOV 2022

Author Contributions:

Conceptualization: Hans-Werner Becker, Sumit Chakraborty
Funding acquisition: Hans-Werner Becker, Sumit Chakraborty
Methodology: Hans-Werner Becker, Sumit Chakraborty
Project Administration: Hans-Werner Becker, Sumit Chakraborty
Supervision: Hans-Werner Becker, Sumit Chakraborty
Writing – original draft: Kendra J. Lynn, Hans-Werner Becker, Sumit Chakraborty

Abstract Studying diffusion of hydrogen in nominally anhydrous minerals, like clinopyroxene, at low temperatures is a challenging task due to experimental and analytical difficulties. In this study, to overcome these problems we have produced H concentration gradients in single crystals of natural diopsidic clinopyroxene by ion implantation and measured the nanoscale profiles before and after diffusion anneals using Nuclear Resonance Reaction Analysis. These steps allowed us to conduct experiments at temperatures between 195°C and 400°C. Obtained diffusion rates show a consistent Arrhenius relation $D_H = 5.47(\pm 13.98) \cdot 10^{-8} \cdot \exp(-115.64(\pm 11.5)\ \text{kJ mol}^{-1}/\text{RT})\ \text{m}^2\text{s}^{-1}$. Notably, our results lie well within the range of extrapolations from high temperature experiments (≥600°C) of previous studies. This implies that fast diffusion of hydrogen (compared to other elements) extends to low temperatures. We used these results in a non-isothermal diffusion model that simulates the ascent of crystals (0.5, 1.0, and 2.0 mm) along two representative *P-T*-paths from 600°C to 100°C, to assess potential re-equilibration of H contents in clinopyroxene at low temperatures. Our model highlights the need to carefully consider boundary conditions, which are a function of *P-T-f*O_2, that control the concentration gradient at the crystal's rim. The results from this model help to assess, as a function of crystal size and cooling rate, when re-equilibration must be considered.

1. Introduction

The presence of hydrogen (often simplistically termed "water") in nominally anhydrous minerals (NAMs) has considerable implications for our understanding of Earth's dynamics. Properties such as melting (Hirth & Kohlstedt, 1996), electrical conductivity (Fei et al., 2020; Karato, 1990), seismic response (Karato & Jung, 1998), phase transitions (Ohtani & Litasov, 2006), and mechanical features (Chen et al., 2006) of a mineral are affected already by trace amounts of hydrogen. Although measured concentrations of H in NAMs are very low (e.g., a few to several thousand ppm H_2O, typically; e.g., Bell & Rossman, 1992; Le Roux et al., 2021; Warren & Hauri, 2014) compared to those in common hydrous phases, when the hydrogen contents of a single mineral are scaled to a planetary scale it becomes obvious that the amount of hydrogen that might be stored in the mantle would make a large contribution to the earth's overall water budget and cycle (e.g., Hirschmann, 2006; Hirschmann & Kohlstedt, 2012; Kohlstedt et al., 1996; Rossman, 1996; Smyth et al., 1991). Thus, it is not surprising that great efforts have been invested in further exploring the role of hydrogen in NAMs since the early works of Beran and Zemann (1969) on olivine and Skogby and others in clinopyroxenes (Skogby, 1994; Skogby & Rossman, 1989; Skogby et al., 1990), as reflected in *Volume 62* of *Reviews in Mineralogy and Geochemistry* (Keppler & Smyth, 2006) and a vast number of more recent studies (e.g., Demers-Roberge et al., 2021; Ferriss et al., 2018; Jollands et al., 2021; Liu & Yang, 2020; Moine et al., 2020; Padrón-Navarta et al., 2014; Reynes et al., 2018; Thoraval et al., 2019; Tollan et al., 2017).

However, a legitimate question that remains is whether hydrogen concentrations that are measured in NAMs collected on Earth's surface really represent the original H contents established in the mantle, or if these contents were modified at some later stage for example, by alteration, metasomatism (Kilgore et al., 2020; Peslier et al., 2015; Tang et al., 2020) or mineral-melt interaction (Le Roux et al., 2021; Lynn & Warren, 2021). In spite of the growing number of experimental studies that reveal new details on hydrogen in NAMs and systematic studies about hydrogen contents in these minerals (Kumamoto et al., 2019; Warren & Hauri, 2014), studies that treat natural mantle xenoliths seem to yield contrasting results in terms of what the hydrogen content actually recorded (Gose et al., 2011; Wang et al., 2021). Since diffusion controls the redistribution of hydrogen in a crystal it is crucial to determine rates of diffusive transport as a function of various parameters (e.g.,

Writing – review & editing: Kendra J. Lynn, Hans-Werner Becker, Sumit Chakraborty

temperature, pressure, fO_2, or mineral composition) to assess potential modifications of hydrogen contents at different conditions. These quantities are known only by extrapolation of high temperature data because most experimental data for H diffusion in NAMs have been collected only over a limited range of high temperatures (800°C–1200°C for olivine, 600°C–1000°C for pyroxenes; e.g., Demouchy & Mackwell, 2006; Demouchy et al., 2016; Ferriss et al., 2016, 2018; Hercule & Ingrin, 1999; Ingrin et al., 1995; Mackwell & Kohlstedt, 1990; Stalder & Behrens, 2006; Stalder & Skogby, 2003; Woods et al., 2000) and may lead to large uncertainties on extrapolation (Lynn & Warren, 2021).

To quantify the loss/retention of hydrogen at low temperatures (e.g., <<600°C) it is necessary to know the rates of diffusion at those conditions. We combined two experimental methods, ion implantation and Nuclear Resonance Reaction Analysis (NRRA), to develop a method for the determination of diffusion rates of H in NAMs at low temperatures. Hereby we were able to quantify diffusion rates of hydrogen in clinopyroxene at 195°C–400°C, temperatures that are associated with metasomatism, prolonged cooling of lava flows or eruption deposits, and serpentinization and that are relevant for applications such as ascent chronometry (e.g., Demouchy et al., 2006; Jollands et al., 2020; Newcombe et al., 2020). We use non-isothermal diffusion modeling with the newly obtained diffusion rates to assess the feasibility of hydrogen re-equilibration during ascent of clinopyroxene from the mantle.

2. Methods

2.1. Sample Preparation

For our diffusion experiments we used gem quality single crystals of diopsidic clinopyroxene (Cpx 25 in our collection) from Pakistan that was obtained from a gem dealer. These had to have homogeneous surface areas that were free of cracks (to avoid adsorbed water causing artifacts) and could accommodate the ion beam used for NRRA analysis (spot ∅ 1–2 mm). The crystal used had an average formula of $Na_{0.03}Ca_{0.95}Mg_{0.88}Fe^{2+}_{0.08}Fe^{3+}_{0.02}Cr_{0.01}Al_{0.04}Si_{1.98}O_6$ (standard deviation of each formula unit <0.01). The composition was determined using a *Cameca SX Five FE* electron microprobe operated at 15 keV and 15 nA using wavelength dispersive spectrometers (Crystals used: LTAP for Na, Mg, TAP for Al, Si, LPET for K, Ti, PET for Ca, Cr and LLIF for Mn, Fe). Fe^{2+}/Fe^{3+} ratios were estimated following Droop (1987). The standards used were jadeite (Na), San Carlos Olivine (Mg, Si), orthoclase (Al, K), diopside (Ca), rutile (Ti), synthetic Cr_2O_3 (Cr), spessartine (Mn), and fayalite (Fe). The crystallographic orientation was verified by Laue analysis before large prismatic crystals (few cm in length) were cut into several slabs (thickness ∼3 mm) with the surface perpendicular to the crystallographic *c*-axis [001]. Additionally, crystals from the same collection have been studied using the TEM in other thesis projects in our lab and the data show that these are clean clinopyroxenes (e.g., no exsolution or inclusions). The oriented crystals were embedded in epoxy, ground, and finished with a final polishing (to 0.25 µm) using diamond paste. Additional surface preparation (e.g., chemical polishing), as used in other studies in our laboratory (e.g., Müller et al., 2013) was considered not necessary because diffusion in this study was not studied in the near surface region (within few tens of nanometer of the surface). Cuboids with a surface area of about 4 × 4 mm were produced from these polished crystals (Figure 1). Finally, the samples were intensively cleaned using a routine involving deionized water, acetone, and ethanol and checked for the quality of polishing in an optical microscope using reflected light.

2.2. Hydrogen Implantation

Hydrogen was implanted at the 500 kV accelerator at the Central Unit for Ionbeams and Radionuclides (RUBION) at the Ruhr-University Bochum, Germany. The depth of the implantation depends on the ion beam energy and the material-specific stopping-power, *s*, which is an expression for the energy loss of the incident ion per distance unit (e.g., keV/nm). Concentration profiles were simulated using the software SRIM (Ziegler et al., 2010) prior to the actual implantation to determine the best choice of ion beam energy. Ideally, the latter is high enough to produce a concentration peak at depths far from the sample surface so that the profile after diffusion experiments is not (partially) superimposed by the surface peak that is related to adsorption of contaminants on the sample surface. Notably, we observed in another study that the process of preparation can introduce excess hydrogen in the near surface region in olivine (∼first 100 nm, Figure S3 in Supporting Information S1). This aspect does not interfere with the results of our study because (a) the measured hydrogen is on the surface of the crystal rather than in it, and (b) the region of the crystal where diffusion is measured (∼650 nm inside the crystal) is far removed

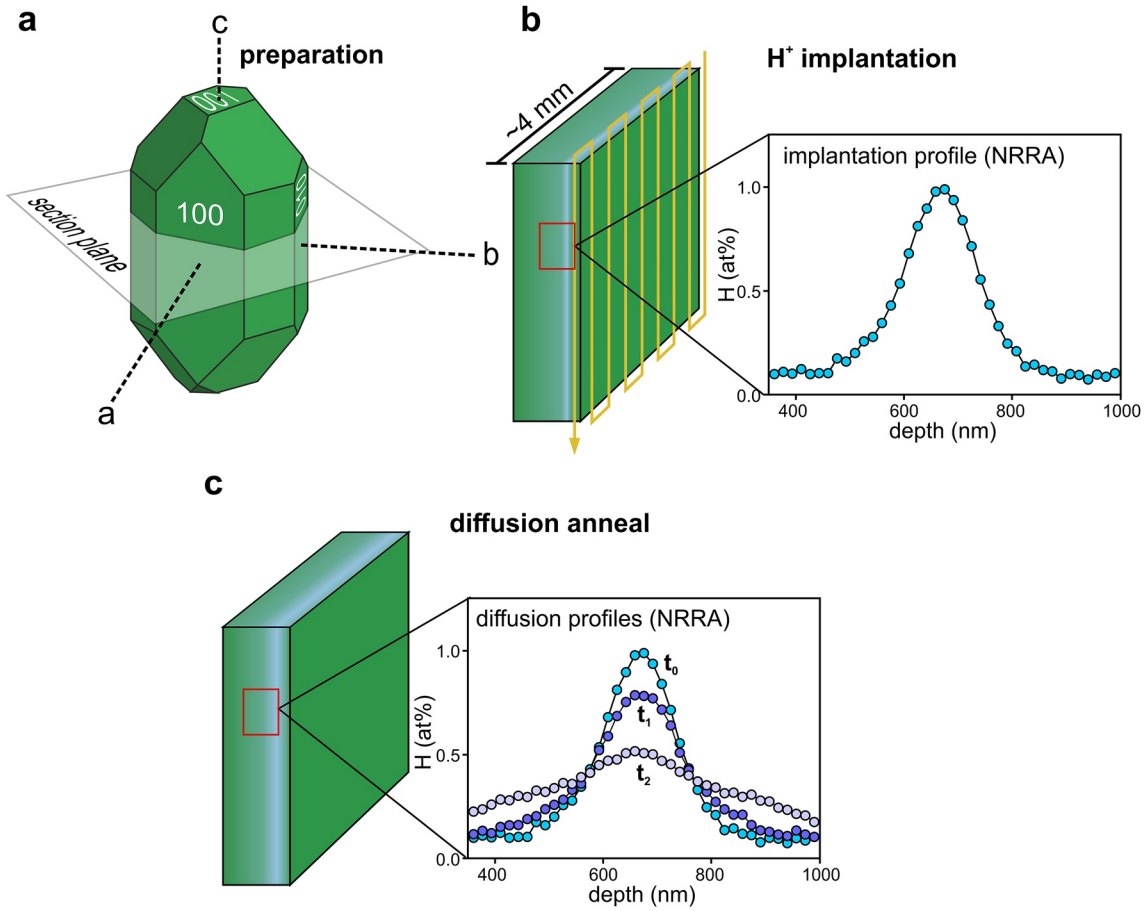

Figure 1. Illustration of the experimental procedure. (a) Diopside crystals were oriented and cuboids with a surface area of ca. 4 × 4 mm were cut with their surfaces perpendicular to the crystallographic *c*-axis (b) Polished sample surfaces were implanted by a hydrogen beam at 60 keV to produce concentration peaks at around 650 nm depth and 1 at% H (1,650 H_2O ppm wt%) concentration maxima. The beam width is larger than the sample size and the implantation is operated in a scanning mode (yellow line). (c) An analysis of the implantation profile by Nuclear Resonance Reaction Analysis (NRRA) to precisely define the initial diffusion setup (t_0) was followed by diffusion anneals at 195°C, 270°C, and 400°C in a gas mixing furnace (100 vol% CO_2). Resulting diffusion profiles were finally measured with NRRA. The non-destructive nature of the experimental design allows to obtain snapshots (profiles t_1 and t_2) of the proceeding homogenization with time. Dimensions are not to scale.

from the region of high H concentration near the surface (~few 10's of nm) (see Figure 1). Additionally, beam energies should be small enough to deposit hydrogen at depths that are still easily accessible using NRRA (max. depth ~2–3 μm). Fluences of $1.48 \cdot 10^{16}$ at/cm^2 were implanted at an ion energy of 60 keV and a beam intensity of 15 μA, while the implantation area was about 1 cm in diameter. The hydrogen source was a duoplasmatron and the ion beam was moved across the sample in a scanning mode during implantation to ensure homogeneous lateral distribution of hydrogen (Figure 1). Implanted concentration maxima were located at around 650 nm from the sample surface.

2.3. Nuclear Resonance Reaction Analysis (NRRA)

Hydrogen concentration profiles that result from implantation and diffusion experiments were measured using NRRA. We limit the information about this method to the essentials and refer the reader to Becker and Rogalla (2016) for a thorough description and to Bissbort et al. (2021) for an explanation in context of a diffusion study. NRRA utilizes the nuclear reaction $^1H(^{15}N,\alpha\gamma)^{12}C$ to detect hydrogen by bombarding the sample with ^{15}N ions. Emitted γ-rays have a specific energy of 4.4 MeV, which is characteristic for this nuclear reaction. The γ-rays are counted using a NaI(Tl) borehole detector with a high detection efficiency. The probability for the nuclear reaction depends strongly on the ^{15}N energy (width of the resonance window is 1.8 keV (Maurel & Amsel, 1983)) with a resonance at 6,393.6 ± 1.3 keV (Osipowicz et al., 1987) or at 6,399.1 ± 2.9 keV (Becker

et al., 1995). ^{15}N at the resonance energy will introduce the nuclear reaction in the very first atomic layers of the sample surface that is, probe the hydrogen content at the surface. An increase in beam energy shifts the nuclear reaction to greater depths, since ^{15}N must loose energy by ion-sample-interaction first to attain the resonance energy. Hence, entire hydrogen depth profiles can be obtained by increasing the beam energy by small increments (e.g., 20 keV) while maintaining the depth resolution of a few nm due to the strong energy-sensitivity of the nuclear reaction. The detected γ-rays are normalized to the incident beam ions (=yield) and are a direct measure of the number of hydrogen atoms, thus making NRRA a standard-less technique. A conversion of the beam energy to a distance unit requires the knowledge of the material-specific stopping-power s, which is a function of the sample composition and density. We used the software SRIM (Ziegler et al., 2010) to calculate the stopping-power for ^{15}N in clinopyroxene of the relevant composition. Dividing the difference between beam energy and resonance energy (ΔE) by the stopping power yields the distance. Typical beam currents during analysis were ~40 nA. NRRA is a nuclear method that is independent of chemical bonds (which depend on outer electrons), thus the total hydrogen content is detected irrespective of its nature of bonding (e.g., H_2, H_2O, $(OH)^-$). One initial calibration is sufficient, and no standards are needed in contrast to alternative methods (e.g., SIMS or IR-spectroscopy) that are often used to measure hydrogen concentration profiles (for details on the calibration see Traeger et al., 2011 and Becker & Rogalla, 2016). Most notably, NRRA is a non-destructive technique that allowed us to measure the initial profile prior to experiments and to observe the development of diffusion profiles with time within one sample.

2.4. Hydrogen Diffusion Experiments

Implantation of hydrogen produced concentration profiles that are approximately described by a normal distribution with depth (depth of implantation maxima ~650 nm), with a minor excess of hydrogen along the surface-facing side of the concentration peak (Figure 2a). Hydrogen concentration depth profiles were obtained by NRRA in each sample after implantation and before diffusion experiments, thereby allowing us to characterize the initial diffusion setup. Diffusion experiments were performed in a gas-mixing furnace using a *K*-type thermocouple (NiCr-Ni). The furnace was flushed with 100 vol% CO_2 to establish non-oxidizing conditions during experiments (it is not possible to control fO_2 at a specific value at the low temperatures of this study by mixing CO and CO_2). Experiments were terminated by dropping the samples in an actively cooled zone for fast quench.

3. Modeling of Hydrogen Diffusion

Diffusion profiles were fitted using an explicit numerical solution. Concentration changes with time at a specific location are described by Fick's second law (Equation 1), with c being the concentration, t being time, x being the distance, and D being the diffusion coefficient. A finite difference scheme was used to solve the diffusion equation (Equation 2), with Δt being the time step size, Δx being the distance step size, c being

$$\frac{\partial c(x,t)}{\partial t} = D\frac{\partial^2 c(x,t)}{\partial x^2} \tag{1}$$

$$c_{i,j+1} = c_{i,j} + \frac{D\cdot\Delta t}{\Delta x^2}\cdot\left[c_{i+1,j} - 2c_{i,j} + c_{i-1,j}\right] \tag{2}$$

$$\sigma_{\text{fit}} = \frac{1}{N}\sqrt{\sum\left(C_{ms}(x) - C_{\text{cal}}(x)\right)^2} \tag{3}$$

the concentration with the two subscripts i and j being indices for space and time, respectively. The geometry of the diffusion problem in this study involves a concentration gradient (i.e., implantation peak) that is located far from the crystal surface (Figure 2). Thus, the system boundaries are unaffected by diffusion (i.e., infinite medium) and are modeled to be open at both ends of each profile. The reader is referred to Costa et al. (2008) for a detailed description of the numerical solution. Notably, the non-destructive NRRA allows us to measure concentration profiles prior to experiments that are used as an initial condition ($t = 0$) in diffusion calculations (i.e., providing $c_{i,0}$ values). This approach provides an ideal description of the diffusion geometry, in contrast to an assumed initial profile (e.g., Gaussian). Finally, this allows to model much smaller changes in hydrogen distribution, and it eliminates the necessity to consider convolution effects.

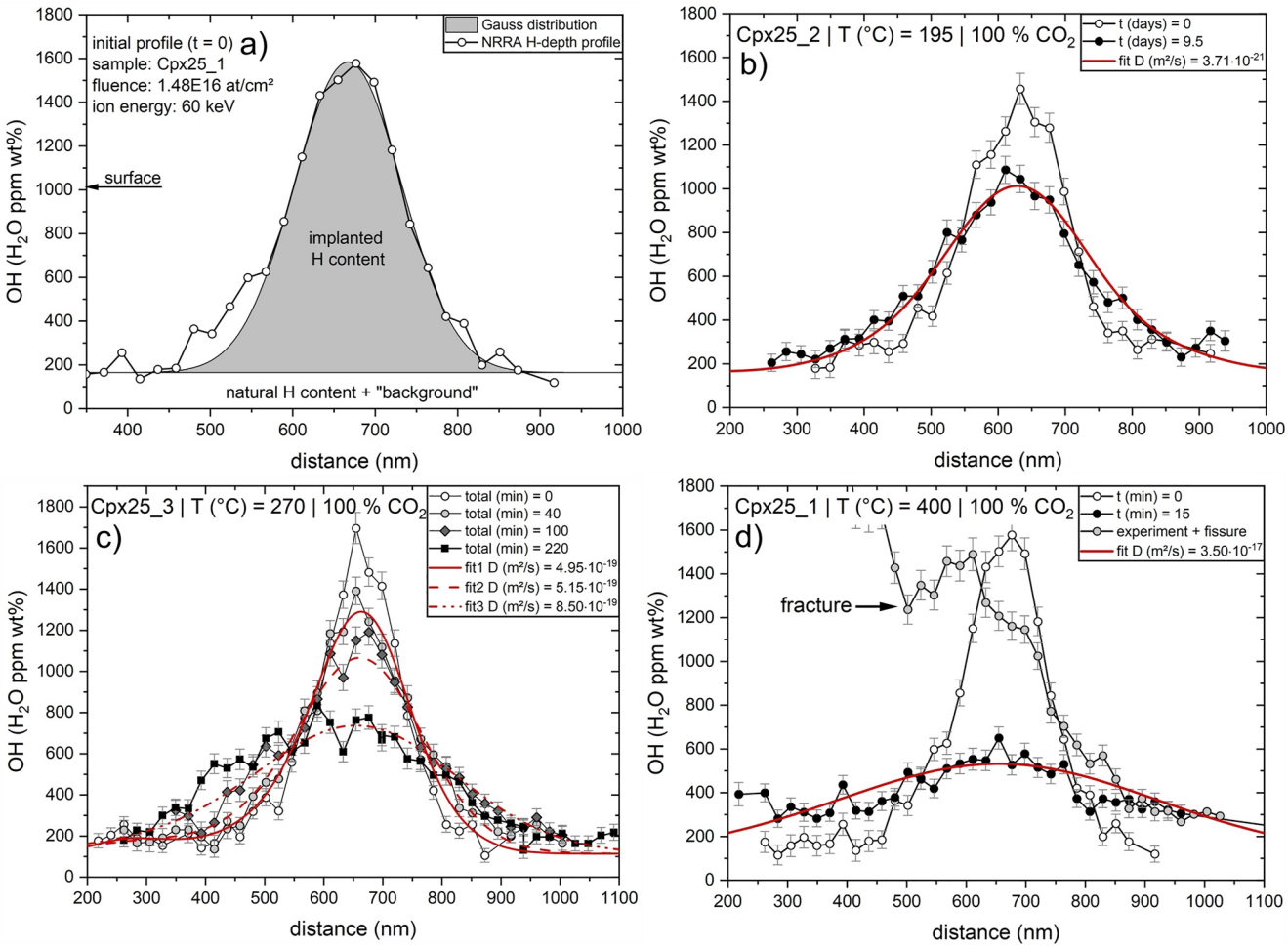

Figure 2. (a) Example for a hydrogen concentration depth profile produced by ion implantation and measured by Nuclear Resonance Reaction Analysis (NRRA) (open circles). The shape of the peak can be described a Gaussian distribution (gray area). (b) The initial hydrogen implantation profile (open circles) broadened and flattened due to diffusion at 195°C for 9.5 days (filled circles). The red line is the best fit of the numerical solution. (c) A time-series was performed in sample Cpx25_3 at 270°C. The obtained diffusion coefficients from best fits display consistency over time. (d) The concentration profile in Cpx25_1 was strongly modified after only 15 min at 400°C. The gray circles illustrate how a depth profile is affected if a fracture loaded with adsorbed atmospheric water interferes with NRRA analysis (i.e., the ion beam spot).

Diffusion of hydrogen at experimental temperatures led to a broadening of the implanted concentration peak while its maximum decreased. The resulting concentration profile could be satisfactorily fitted with a constant diffusion coefficient D along the profile distance at a given temperature, which indicates that there is no observable dependence of diffusion rates on hydrogen concentration. Experiments were conducted at three different temperatures, 195°C, 270°C, and 400°C (Figures 2b and 2c). A timeseries of 3 experiments within one sample (Cpx25_3) at 270°C gives insight on how the diffusion profile develops within one sample with increasing experimental duration. It was also used to assess the suitability of our method for obtaining diffusion coefficients, which is supported by almost constant diffusion coefficients ($\Delta \sim 0.24$ log units, Figure 3) in this time-series. D values were constrained by minimizing the misfit (σ_{fit}) between each measured concentration, $c_{ms}(x)$, and the corresponding calculated concentration, $c_{cal}(x)$ at the same location (Equation 3). A summary of the experiments, determined diffusion coefficients, and misfit σ_{fit} is provided in Table 1.

4. Comparison With Previous Studies

Diffusion rates that were determined in our experiments describe an Arrhenius relation $D_H = 5.47\ (\pm 13.98) \cdot 10^{-8} \cdot \exp\ (-115.64\ (\pm 11.5)$ kJ mol^{-1}/RT) m^{2}s^{-1} (purple solid line, Figure 4). Our experimental method allowed us to explore diffusion of hydrogen in diopside (X_{Fe} = Fe/(Fe + Mg) = 0.102) at low temperatures (195°C–400°C).

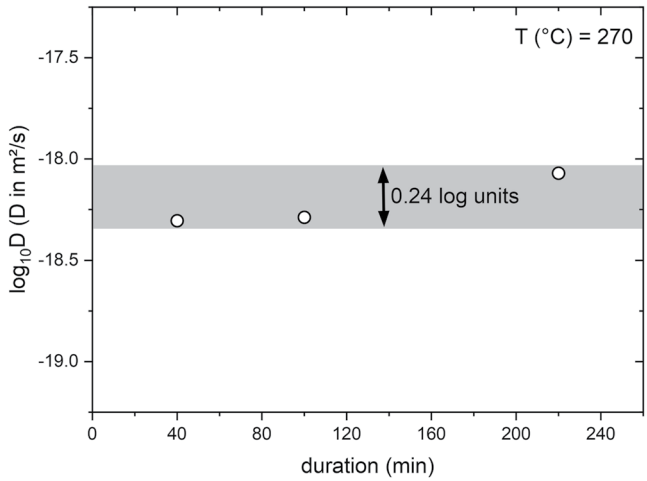

Figure 3. Diffusion coefficients that were obtained from fitting concentration profiles from the time-series at 270°C yield constant values over time. The range of scatter in $\log_{10}D$ is about 0.24 log units and is larger than error estimates calculated from error propagation. For further details see Appendix A in Faak et al. (2013).

However, a comparison of our results with those of other studies in clinopyroxene is restricted to higher temperatures (≥600°C).

Ingrin et al. (1995) conducted dehydration experiments in Russian gem quality diopside (X_{Fe} = 0.036) crystals at 700°C–1000°C in air. They studied diffusion along three crystallographic directions, [001], [100]*, and [010] using FTIR but did not find anisotropy in diffusion rates. Thus, they propose that diffusion of hydrogen is isotropic in diopside. The temperature dependence, which is valid for all orientations, is expressed by an Arrhenius relation $D_H = 5.04(\pm14.12) \cdot 10^{-7} \cdot \exp(-136 \pm 27$ kJ mol^{-1}/RT) m^2/s (gray solid line, Figure 4).

Instead of dehydration experiments, Hercule and Ingrin (1999) performed extraction-incorporation experiments in diopside crystals similar to those used in Ingrin et al. (1995) at 700°C–1000°C at a pH_2 of 0.1 and 1 atm. Similar to Ingrin et al. (1995) they observe that the kinetics are independent of crystallographic orientation, but also of the partial pressure of H_2 and oxygen fugacity fO_2. They determined an Arrhenius law $D = 2.00\ (\pm5.05) \cdot 10^{-7} \cdot \exp(-126 \pm 24$ kJ mol^{-1}/RT) m^2/s for this set of experiments (green dotted line, Figure 4). The authors also carried out hydrogen-deuterium exchange experiments in the same diopside at 600°C–900°C along [001], [100]*, and [010] at 1 atm. They observe that diffusion along [001] and [100]* is two orders of magnitude faster than the incorporation rate from the other experimental setup. The Arrhenius relation is $D_H = 3.98\ (\pm7.33) \cdot 10^{-4} \cdot \exp(-149 \pm 16$ kJ mol^{-1}/RT) m^2/s (green dashed line, Figure 4). Diffusion along [010] is slower than in the other directions but one magnitude faster than the H uptake. The related Arrhenius law is $D_H = 1.00\ (\pm3.91) \cdot 10^{-5} \cdot \exp(-143 \pm 33$ kJ mol^{-1}/RT) m^2/s (green solid line, Figure 4). They conclude that incorporation of hydrogen is coupled to oxidation-reduction of iron $Fe^{3+} + O^{2-} + 1/2H_2\ (g) = Fe^{2+} + OH^-$. Hence, the rate of hydrogen uptake is a function of the crystals Fe-content (Hercule & Ingrin, 1999).

Woods et al. (2000) used Jaipur diopside crystals (X_{Fe} = 0.069) for dehydration experiments between 700°C and 850°C and at fO_2 of 10^{-14} bar. A comparison of diffusion rates between crystallographic orientations shows that rates along [100] and [001]* are fastest with the Arrhenius relations $D_H = 7.94\ (\pm34.75) \cdot 10^{-3} \cdot \exp(-181 \pm 38$ kJ mol^{-1}/RT) m^2/s (yellow dashed line, Figure 4) and $D_H = 3.98\ (\pm14.67) \cdot 10^{-4} \cdot \exp(-153 \pm 32$ kJ mol^{-1}/RT) m^2/s (yellow solid line, Figure 4), respectively. The relatively narrow experimental temperature range did not allow them to obtain a temperature-relation for diffusivity along [010]. However, their experiments indicate that diffusion along [010] is an order of magnitude slower than in the other two directions. The observed anisotropy agrees with the results from Hercule and Ingrin (1999). Woods et al. (2000) point out that mm-size diopside crystals will be affected by re-equilibration at temperatures as low as 800°C.

Sundvall et al. (2009) used Fe-free diopside ($X_{Fe} \approx 0.0$) that was synthesized at water-saturated conditions. Their results from FTIR analysis of dehydration experiments at 800°C–1000°C indicate that diffusion rates along [010] and [100]* are similar within error limits, which contradicts previous studies mentioned above. The Arrhenius relation for [010] is $D_H = 7.94\ (\pm42.07) \cdot \exp(-331 \pm 50$ kJ mol^{-1}/RT) m^2/s (pink solid line, Figure 4). Diffusion rates along [100]* exhibit an Arrhenius relation $D_H = 3.16\ (\pm17.48) \cdot \exp(-312 \pm 55$ kJ mol^{-1}/RT) m^2/s (pink dashed line, Figure 4). These diffusion rates are several orders of magnitude slower than in natural Fe-bearing samples. This difference also applies to diffusion rates we obtained in our natural diopside crystals when one extrapolates the high temperature data to low temperatures (pink lines, Figure 4).

Ferriss et al. (2016) studied dehydration in Kunlun diopside (X_{Fe} = 0.025), Jaipur diopside (X_{Fe} = 0.075), and augite (X_{Fe} = 0.180) at 800°C–1000°C at an fO_2 at the QMF buffer. They present an Arrhenius relation for isotropic hydrogen diffusion in Kunlun diopside $D_H = 1.59\ (\pm31.02) \cdot 10^{-9} \cdot \exp(-100.4 \pm 2.7$ kJ mol^{-1}/RT) m^2/s (blue solid line, Figure 4). Experiments in the Jaipur diopside and augite, which are more Fe-rich than the Kunlun

Table 1
Diffusion Experiments at 195°C, 270°C, and 400°C

Sample_experiment	T (°C)	Total duration	D (m^2/s)	σ_{fit}
Cpx25_1_EXP1	400	15 min	$3.50 \cdot 10^{-17}$	0.015
Cpx25_2_EXP1	195	9.5 days	$3.71 \cdot 10^{-21}$	0.006
Cpx25_3_EXP1	270	40 min	$4.95 \cdot 10^{-19}$	0.007
Cpx25_3_EXP2	270	100 min	$5.15 \cdot 10^{-19}$	0.010
Cpx25_3_EXP3	270	220 min	$8.50 \cdot 10^{-19}$	0.006

Note. For the timeseries the total duration is the sum of the dwell time.

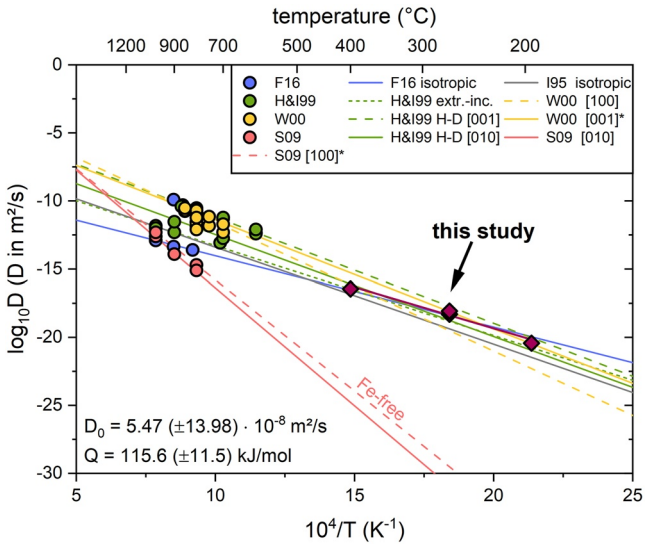

Figure 4. A comparison of published diffusion coefficients from high temperature experiments ($T \geq 600$°C) and associated Arrhenius relations (colored lines) with results from this study (purple data, error bars smaller than symbols) confirm that latter lie well within the $\log_{10}D$ range predicted by extrapolation from high temperatures. F16 = Ferriss et al. (2016); H&I99 = Hercule and Ingrin (1999); W00 = Woods et al. (2000); S09 = Sundvall et al. (2009); I95 = Ingrin et al. (1995).

diopside, show faster diffusion of hydrogen at the same temperature. This suggests that higher Fe contents cause faster diffusion rates of hydrogen. The authors also compare diffusion rates of hydrogen between clinopyroxenes of various Fe contents, including other studies. There is an increase in diffusion coefficients with increasing Fe-contents, but this increase diminishes toward high Fe contents. As pointed out by Ferriss et al. (2016), a compositional dependence of hydrogen diffusion in clinopyroxene might not be adequately described by the Fe content, instead Al could also play a significant role as has been shown for orthopyroxene by Kumamoto et al. (2019). Unfortunately, they do not provide Arrhenius relations for the Jaipur diopside and augite, which precludes a direct comparison of results from these samples with results of our study. However, an extrapolation of the Arrhenius law that was obtained for the Kunlun diopside is in excellent agreement with our results, although X_{Fe} is much higher in our diopside (0.102 vs. 0.025). The conformity of diffusion rates in our diopside and the Kunlun diopside despite substantially different Fe contents (X_{Fe} of our sample lies between that of the Jaipur diopside and augite) also indicates a more complex composition-diffusivity relationship.

A comparison of our diffusion rates with extrapolations from previous studies at high temperatures, highlights that we were able to resolve the outstanding issue whether diffusion rates can be extrapolated from high temperatures toward low temperatures. Our results lay well within the range that is constrained by extrapolation of Arrhenius relationships from high temperature experiments for Fe-bearing diopside to temperatures relevant in this study (Figure 4). Although, we did not constrain diffusion rates as a function of crystal orientation, previous studies (e.g., Hercule & Ingrin, 1999; Woods et al., 2000) suggest that diffusion coefficients along [001] are greatest and like those along [100]. Therefore, it is evident that the high diffusivity of hydrogen (compared to other elements) in clinopyroxene extends continuously toward low temperatures.

Further, diffusion profiles in our experiments are well fitted by a simple (i.e., concentration-independent) numerical diffusion model (solving Fick's second law, Equation 1) and diffusion rates as a function of temperature describe an Arrhenius relation. The consistency of our results resolves two concerns that might arise when implanted concentration distributions are to be used for diffusion studies. (a) Does the damage introduced by ion implantation affect diffusion? (b) Is the implanted hydrogen bonded to the mineral matrix like "natural" hydrogen? First, hydrogen is a light element and therefore causes less damage during implantation compared to heavy elements at low energies (Zhang et al., 2009). Further evidence for a negligible damage of the sample is provided by results of diffusion experiments. Sample damaging (i.e., introduction of defects) due to irradiation follows a distribution similar to that of the hydrogen concentration. Thus, the region between the sample surface and the end of the implantation peak is affected by irradiation damage, but not so the rest of the sample at greater depth. If irradiation damage is thought to be intense enough to affect diffusion to a non-negligible extent, one would expect this to be reflected in an asymmetric development of the concentration profile, caused by a different diffusion rate and/or mechanism in the damaged zone compared to the pristine crystal. This was not observed in our diffusion profiles (Figure 2). Regarding (b), IR-measurements of implanted hydrogen in olivine confirm that all the implanted hydrogen is present as OH, similar to the bonding state of natural hydrogen (Schaible & Baragiola, 2014). In this work we assume that clinopyroxene behaves the same way. Hypothetically, a change from H or H_2 to OH during annealing in diffusion experiments would be expected to be accompanied by a change in diffusion rate with time as the proportions of different H-species change. However, time-series experiments feature a constant diffusion rate within uncertainties (Figure 3). Last, implanted hydrogen fluences of $1.48 \cdot 10^{16}$ at/cm^2 are relatively low (peak maximum ~1 at% H; 1,650 wt. ppm H_2O) but close to natural concentrations in mantle pyroxenes (e.g., Warren & Hauri, 2014).

5. Evaluation of Re-Equilibration of H in Clinopyroxene at Temperatures Below 600°C

5.1. A Non-Isothermal Diffusion Model

The newly determined diffusion rates at low temperatures offer us the opportunity to model changes in hydrogen concentrations in clinopyroxene due to diffusion at conditions that are relevant for late-stage hydration and dehydration. Diffusive flux occurs when there is a cause that is, chemical disequilibrium, caused, for example, in response to changes in temperature, pressure, oxygen fugacity (fO_2), the speciation of accompanying fluids, and solubility of hydrogen in clinopyroxene while a crystal of clinopyroxene ascends from the mantle to Earth's surface, for example, in volcanic rocks such as kimberlites or during the process of emplacement of an ophiolite. We have developed a model that simulates diffusion of hydrogen in clinopyroxene during its ascent, while the system variables change according to temperature-pressure paths and associated conditions.

Diffusion is calculated as a temperature dependent process (non-isothermal). The diffusion equation is solved using a finite difference model as described in Section 3. The diffusion coefficient D_H changes during the calculation according to the change in temperature during ascent and is derived from our Arrhenius relation $D_H = 5.47\ (\pm 13.98) \cdot 10^{-8} \cdot \exp(-115.64\ (\pm 11.5)\ \text{kJ mol}^{-1}/\text{RT})\ \text{m}^2\text{s}^{-1}$. Possible effects of pressure and fO_2 on the diffusion coefficient are not included as the former is expected to be weak and the latter is not constrained experimentally, so that we do not have an fO_2-exponent value to use. However, the variation of pressure and fO_2 in the surroundings plays an important role in the calculation through their influence on the boundary conditions. In our model we illustrate the effect using a C-O-H fluid (carbon saturated) that surrounds the clinopyroxene crystal as it moves along a specified *P-T* trajectory, with fO_2 set to vary along the QMF buffer. The associated fH_2O affects the solubility of OH in clinopyroxene (Keppler & Bolfan-Casanova, 2006). Boundary concentrations are adjusted to the appropriate values of hydrogen concentration corresponding to the *P-T-*fO_2 condition at the rim of the crystal at each time step. The initial condition is taken to be a homogeneous hydrogen distribution in the crystal at equilibrium at the *P-T-*fO_2 condition of the starting depth.

The degree of re-equilibration was calculated using Equation 4 where c_{initial} is the initial concentration, $c_{\text{model core}}$ is the maximum concentration after cooling (usually in the core), and c_{eq} corresponds to the final equilibrium concentration (i.e., the concentration at the rim of the crystal) (Chakraborty & Ganguly, 1991; Costa et al., 2003; Lynn et al., 2017).

$$\text{re}-\text{equilibration}\,(\%) = \frac{c_{\text{initial}} - c_{\text{model core}}}{c_{\text{initial}} - c_{\text{eq}}} \times 100 \tag{4}$$

The results provide an impression of how the hydrogen budget and its distribution in clinopyroxene is modified and how this depends on the exhumation history and crystal size. We aim to clarify what the possibilities are in terms of hydrogen re-equilibration, demonstrated through some representative calculations, rather than to reproduce and resolve specific geological scenarios. Therefore, two *P-T-*fO_2-paths were calculated that are taken to lie along a continental (CT, 534°C/GPa) and an oceanic (OC, 226°C/GPa) geotherm, respectively. A detailed description of the development of this model is provided in Appendix I. We underscore that these geotherms are taken merely as examples of two *P-T* trajectories along which we model the H-content evolution of clinopyroxene crystals, and not to describe any particular process. However, the approach that is developed may be used for any natural system with variation of *P* and *T* along any trajectory. Non-isothermal diffusion of hydrogen was modeled for clinopyroxene crystals of 2, 1, and 0.5 mm from 600°C to 100°C and the cooling rate (i.e., ascent rate) was varied by orders of magnitude (1,000–0.1°C/yr) to study its effect on the progress of equilibration. Figure 5 displays both *P-T* trajectories whereas the modeled temperature range is indicated by dashed lines. The calculated geotherm using parameters for a continental lithosphere (CT) yields higher temperatures compared to the oceanic geotherm (OC) at same pressures, due to the assignment of higher radiogenic heat production to the former and a thin oceanic crust of 10 km to the latter (instead of 40 km, see Appendix A for more details).

Although diffusion rates that were derived from the experimentally established Arrhenius relationship are the same for both geotherms at similar temperature ($D = f(T)$), the pressure and therefore the solubility of OH in the model clinopyroxene is different. Consequently, the starting point at 600°C corresponds to a higher pressure of 2.35 GPa for the oceanic and a lower pressure of 1.11 GPa for the continental model geotherm, which corresponds to 70.1 and 45.5 wt. ppm H_2O, respectively. This difference is reflected in the initial state of our models

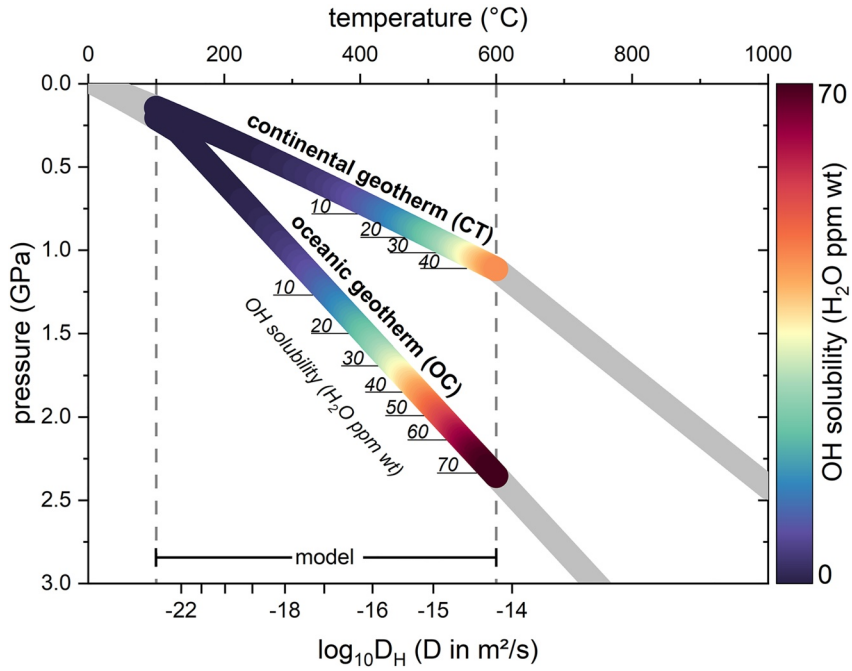

Figure 5. A continental geotherm (CT), an oceanic geotherm (OC), and solubilities of hydrogen in clinopyroxene that correspond to conditions along these PT paths (indicated by number labels and color) were calculated following the procedure described in Appendix. Diffusion rates in our model change during ascent according to the Arrhenius relationship obtained in this study (i.e., non-isothermal). Boundary concentrations that induce a concentration gradient change according to the solubility. Temperature boundaries of the model are indicated by dashed lines (600°C–100°C).

($t = 0$) by a homogeneous concentration plateau and boundary concentrations at these values (Figure 6, dotted lines). A comparison of the evolution of hydrogen diffusion profiles in crystals of similar size that followed different *P-T*-paths reveals that at the same cooling rate the hydrogen content in the clinopyroxene that traveled along CT is more re-equilibrated than one that followed OC. This contrast is a consequence of different OH solubilities along the two paths that define the boundary concentrations (i.e., a compositional gradient), but not a result of different diffusivities. To further test the effect of solubility of OH on the progress of re-equilibration, we changed the boundaries to a fixed low concentration (=0 wt. ppm) right from the start of diffusion process until the final state is attained. We have done this for a cooling rate of 100°C/yr in 1 mm crystals along both *P-T* trajectories (Figure 6, dashed lines). The obtained concentration profiles display an overall different shape compared to the original model that includes variable boundary concentrations. Steeper flanks toward the crystal surface are caused by a steep concentration gradient, which is present from the initial state, and which promotes a strong diffusive flux. Most notably, the extent of re-equilibration proceeded much more when the model did not include solubility-controlled boundary concentrations. Thus, a consideration of not only diffusivities, but of the system variables such as fluid composition (or, more generally, P-T-fO_2-fH_2O conditions in the surrounding medium) that finally control OH solubility in the mineral is necessary to obtain trustworthy estimates on ascent rates or to assess the degree of re-equilibration. On the other hand, details of the profile shapes contain information on how the boundary conditions evolved with time—this may be helpful in setting the boundary conditions for modeling natural profiles.

5.2. Geological Implications

Hydrogen concentration profiles that result from non-isothermal diffusion modeling illustrate that below some threshold in cooling rate (the absolute value of which depends on the nature of the surrounding medium) for a given grain size the initial core concentration is no longer preserved. Small crystals at slow ascent rates show advanced re-equilibration, which is reflected by flat concentration profiles at low values (Figure 6). These should not be misinterpreted to be a sign for low water contents of the mantle, but to be results of a combination of relatively fast diffusion of hydrogen in clinopyroxene even at low temperatures and low H solubilities at those

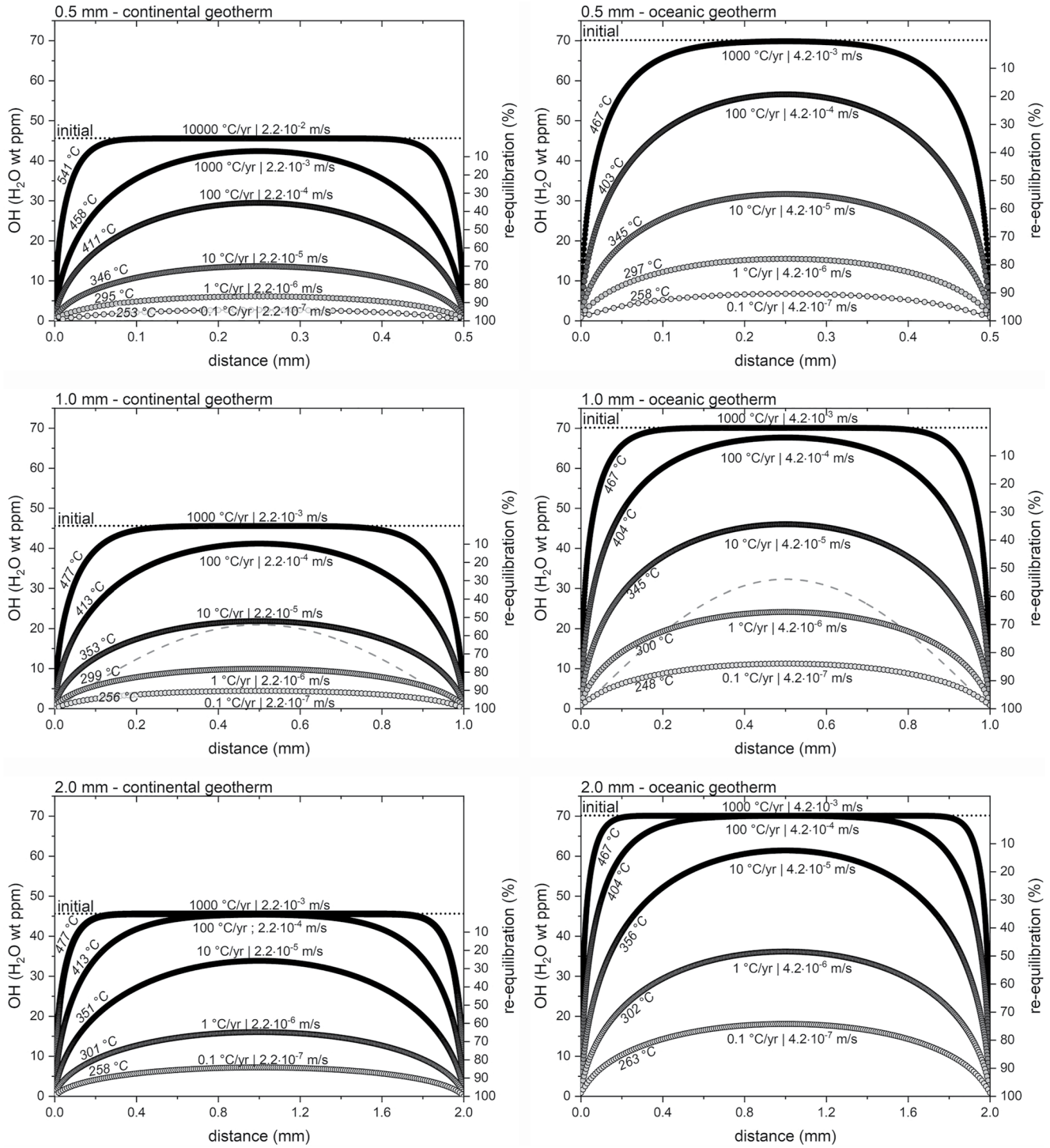

Figure 6. Diffusion profiles calculated from our model for the continental geotherm (continental lithosphere [CT], left side) and the oceanic geotherm (OC, right side) for crystal sizes of 0.5, 1.0, and 2.0 mm (top to bottom) using various cooling/ascent rates. The initial homogeneous OH concentration corresponds to the solubility of OH in clinopyroxene at the starting condition ($T_0 = 600$°C and corresponding pressure) and is indicated by the dotted line (~46 wt. ppm for CT, ~70 wt. ppm for OC). Temperature labels below and above the profiles are apparent closure temperatures as a function of the cooling rate (taken from equilibrium temperatures corresponding to concentrations at 15 µm from the surface). The gray dashed lines in the 1.0 mm models are calculated concentration profiles for a cooling rate of 100°C/yr, but the boundary concentrations were in this case set to the final concentration (at $T = 100$°C) right from the beginning. The substantial differences in shape and extent of re-equilibration compared to the changing boundary concentration model emphasizes the influence of concentration gradients on the rate at which concentration profiles change.

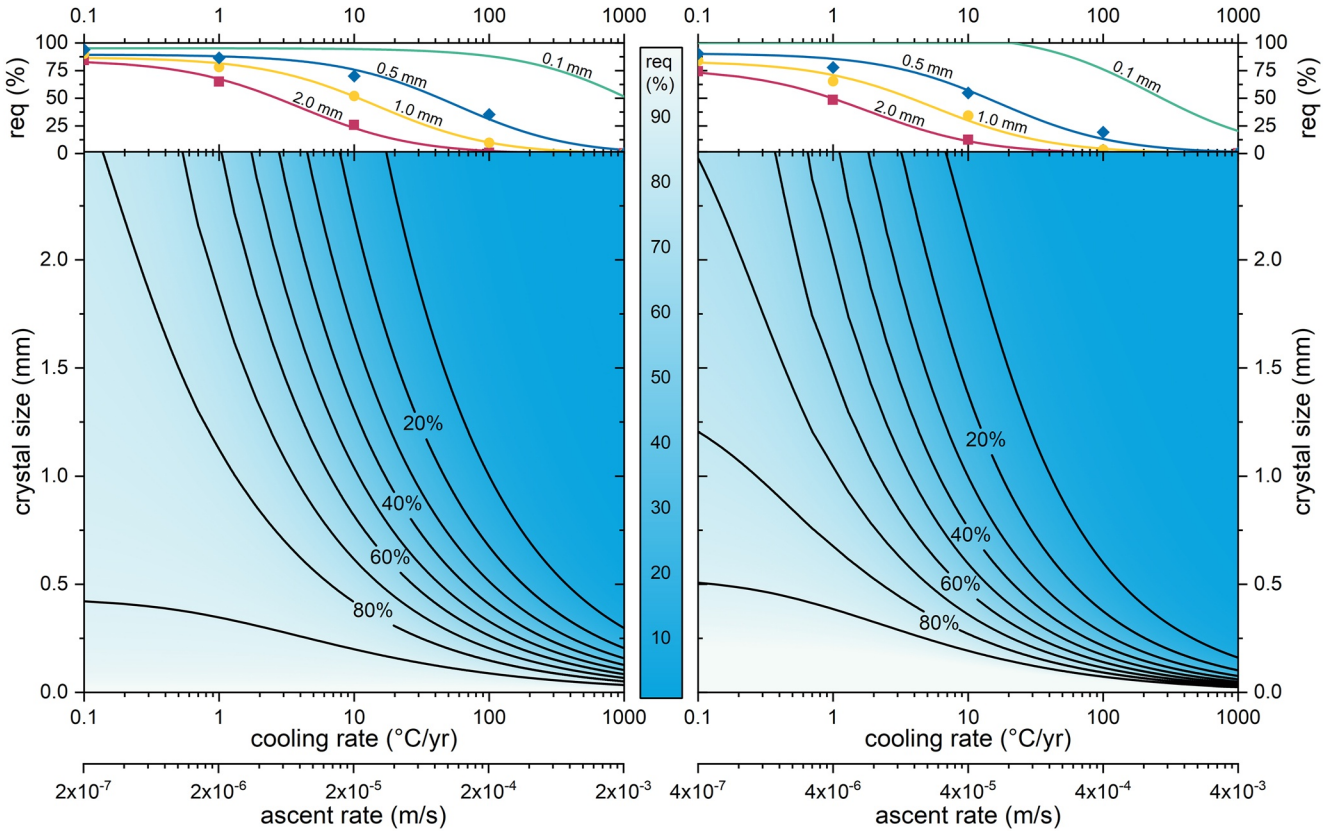

Figure 7. Re-equilibration (req) mapped as a function of crystal size and cooling rate/ascent rate for the continental geotherm (left) and the oceanic geotherm (right). Contours in both maps represent the extent of re-equilibration along these lines. The color gradient visualizes the re-equilibration (blue = OH content preserved; white = completely re-equilibrated). The plotted lines at the top are re-equilibration profiles for 0.1 mm (green), 0.5 mm (blue), 1.0 mm (yellow), and 2.0 mm (pink) obtained from the model (Equation 5). Symbols are the re-equilibration values calculated from the modeled diffusion profiles.

conditions. The dependence of re-equilibration on crystal size and cooling rate follows a systematic behavior that can be described by Equation 5 for each *P-T* trajectory with the crystal size *sz* in mm, the cooling rate *cr* in °C/yr, and the fitting parameters *p1a*, *p1b*, *q1a*, *q1b*, *q2a*, and *q2b* (full description in Appendix B). This equation provides a tool to estimate the progress of re-equilibration for the range of crystal sizes and cooling rates for a given *P-T*-path, if the surrounding medium is a C-saturated C-O-H fluid (Figure 7).

$$\text{re}-\text{equilibration}\,(\%) = \frac{p1a \times sz^{p1b}}{cr^2 + q1a \times sz^{q1b} \times cr + q2a \times sz^{q2b}} \tag{5}$$

These calculations have important geological implications, which we discuss below in the context of (a) ascent chronometry and (b) water contents in NAMs as signature of a mantle source.

(a) Fast diffusion of hydrogen in NAMs has been identified to be a promising tool to model ascent/decompression rates of magma (Newcombe et al., 2020) or to estimate eruption timescales in volcanic settings (Jollands et al., 2020). The principles of the method are that once an initial equilibrium water concentration was determined (either from water concentrations in melt inclusions and K_D(NAM/melt) or directly from preserved hydrogen concentration plateaus in crystal cores) and concentration profiles that result from dehydration are measurable, diffusion modeling can be applied to constrain ascent rates. Our model indicates that even very small clinopyroxene crystal sizes (<0.1 mm) potentially preserve original water contents at their cores at the lower boundary values for estimates on typical ascent rates in volcanoes (e.g., 0.05 MPa/s) and temperatures below 600°C. This implies, that the hydrogen distribution that results from diffusion in NAMs that travel along an adiabat (as an approximation to transport in a melt during ascent), are "frozen in" at relatively high temperatures (Figure 8, left). A modification of these at shallow depths are therefore less likely, and the measured profiles can be interpreted to record ascent rates at high temperatures. However, the uncertainty that is introduced by the choice of

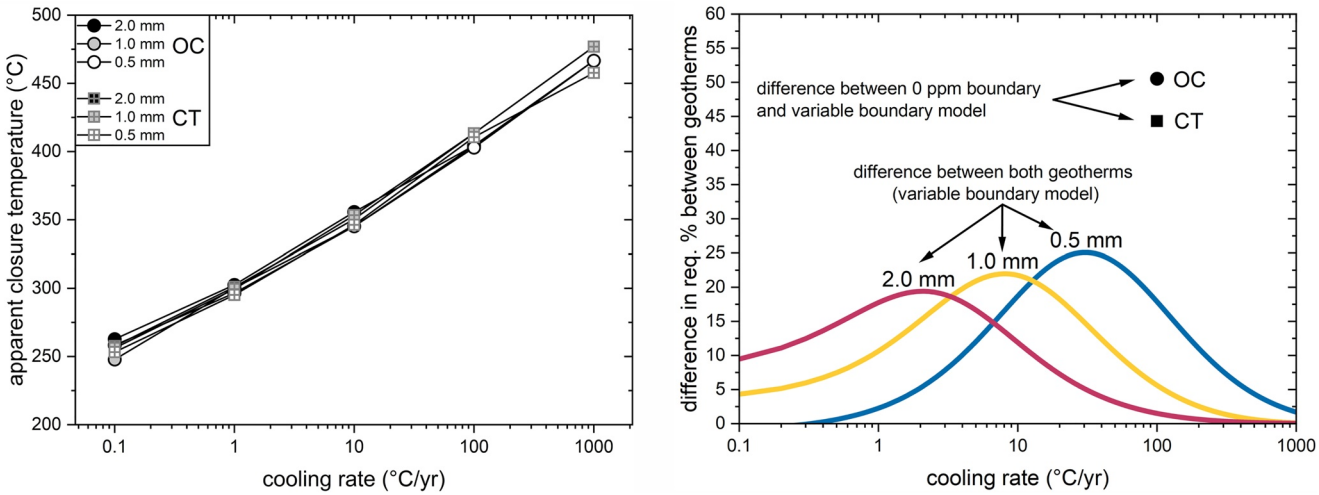

Figure 8. (Left) freezing temperature as a function of cooling rate. Clinopyroxene crystals that were transported in a melt during ascent in volcanic settings are expected to experience fast cooling (>1,000°C/yr) and therefore preserve a hydrogen distribution that was established at higher temperatures. Slow exhumation (i.e., slow cooling) allows the modification of hydrogen distribution within nominally anhydrous minerals in response to lower equilibrium contents at the mineral boundary at low temperatures. (Right) Differences in re-equilibration between the two geotherms for different crystal sizes and as a function of cooling rate (lines). In general, differences in the degree of re-equilibration between crystals of the same size but that traveled along different geotherms are smaller for larger crystals. However, this is complicated by a dependence on cooling rate. At low cooling rates larger crystals display greater differences in the degree of re-equilibration between both geotherms. Notably, setting the boundary concentration to a constant value of 0 ppm (instead of a variable boundary concentration) introduces large differences in the degree of re-equilibration (symbols).

boundary concentrations that induce a concentration gradient can be very large. For example, a simplification of the problem to a scenario in which dehydration corresponds to a large concentration gradient from the beginning (e.g., 0 ppm) produces overestimates on the order of an order of magnitude or so in cooling rates (see Figure 6, dashed lines in 1 mm profiles, Figure 8, right) for the surrounding medium that was used in our model. Our model highlights that when changing boundary concentrations are applied, which are a better approximation to natural cases, the uncertainty in the determined cooling rates can be substantially reduced (Figure 8). Our model is set up for calculating ascent in any system (e.g., volcanoes or emplacement of massive lherzolites), but the boundary conditions in the model would need to be set according to the nature of the surrounding medium, and if it is not a C-O-H fluid then Equation 5 would not apply (new calculations would be required to produce the equivalent of Equation 5).

(b) The finding that NAMs from mantle xenoliths contain hydrogen led to the conclusion that these contents represent hydrogen contents that are in equilibrium with a mantle source (Bell & Rossman, 1992). Although NAMs incorporate only trace amounts of hydrogen, their major abundance in the mantle implies a large contribution to Earth's overall hydrogen budget and cycle. The effect hydrogen has on various properties of minerals (e.g., rheology and melting temperature) highlights the importance of carefully evaluating its abundance in mantle phases. Our results provide a basis to assess whether original hydrogen contents associated with a mantle source can be preserved during ascent or might be modified, or even completely erased. This helps to evaluate whether measured hydrogen concentrations in these natural samples can be interpreted as a mantle signature. Figure 7 shows that mantle xenoliths that were transported to the surface in a kimberlitic magma probably preserved the original hydrogen content due to the fast ascent rates (e.g., 5–37 m/s, Peslier et al., 2008), even if their rim concentrations adjusted continually to decreasing pressure-temperature conditions. In the event that the rim composition is buffered to some value by its surroundings, the extent of resetting would be even less (for the same *P-T* trajectory). This means that OH concentrations that were measured for example, by Bell and Rossman (1992) from a kimberlite source and by Peslier and Bizimis (2015) from Hawaiian peridotite are likely those of a mantle source. However, slow cooling or dwelling at temperatures that are typical for serpentinization (~300°C, Guillot et al., 2015) can erase a mantle signature in large crystals (2 mm) in a few thousand years (Figure 9, left). Results from modeling hydrogen diffusion in clinopyroxene at 300°C illustrate the development of the hydrogen distribution at temperatures associated with serpentinization, a process that was first suggested by Lynn and Warren (2021) and is supported by the newly obtained low-temperature diffusivity constraints here.

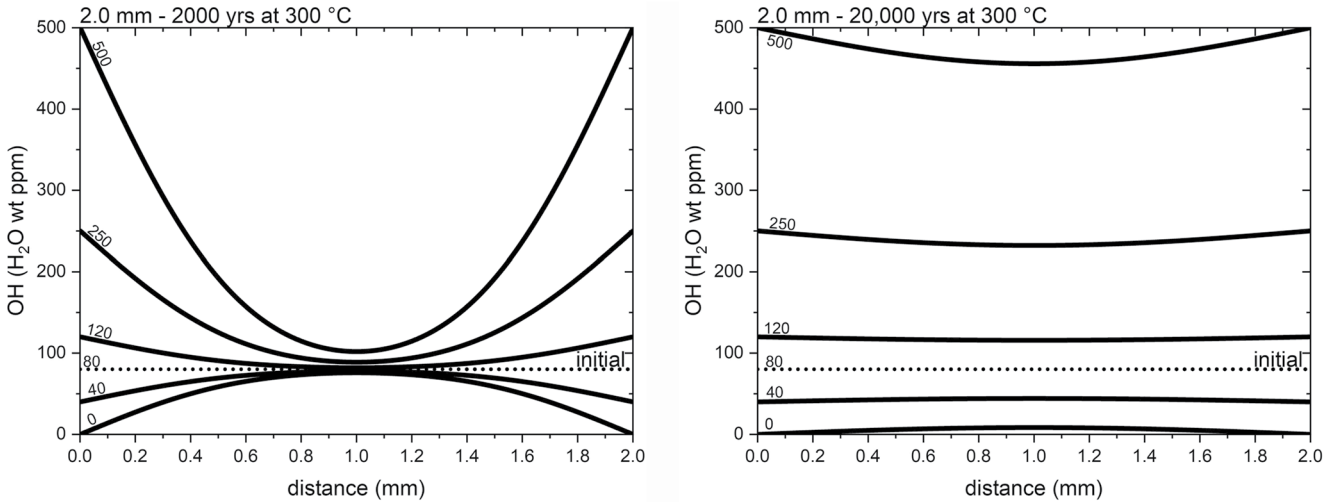

Figure 9. Modeling of isothermal diffusion at 300°C for a 2 mm crystal with constant boundary concentrations that mimics dwelling at a temperature that is characteristic for serpentinization. The initial OH concentration (dotted line) is set to 80 OH (H_2O wt ppm) Using different fixed boundary concentrations (numbers above and below profiles) highlight their influence on the progress of re-equilibration and change in profile shape. (Left) Notably, the core concentration is in almost all cases preserved after 2,000 years although boundary concentrations are very high (e.g., 500 wt ppm). However, concentrations in the rim have substantially changed. (Right) The original hydrogen content almost completely re-equilibrated to the boundary concentration after 20,000 years at 300°C.

As an example, after 2,000 years at 300°C, diffusion strongly modifies the distribution from rim to core, while the core content is almost preserved (dependent on the boundary concentration). Although, a mantle signature could have been preserved in the core, the result highlights the requirement for a careful analysis of core contents. Accurate measurements should prevent integration of hydrogen contents from the either dehydrated or hydrated rim. Finally, after 20,000 years at 300°C the original hydrogen concentration is almost completely homogenized (Figure 9, right); these effects are stronger in smaller crystals/diffusion domains (note that the distance to nearest source of hydration/dehydration, e.g., a crack, is relevant in this context rather than the size of a grain).

While the above results follow from the experimental data that we have obtained, there are intriguing examples of slowly cooled rocks containing high H bearing clinopyroxenes (Katayama et al., 2006; Konzett et al. (2008); Urann et al. (2022)). These may be effects of composition of the clinopyroxenes, shielding by other phases (i.e., the nature of the surrounding medium—please see the discussion above), or the activation of different diffusion mechanisms—these will need to be studied through future work.

6. Conclusion

Diffusion experiments at low temperatures (195°C–400°C) and non-isothermal modeling has resulted in the following conclusions:

1. We applied an experimental and analytical procedure that enables us to study diffusion of hydrogen in clinopyroxene at low temperatures (≤400°C). It was possible to circumvent previous hindrances by using ion implantation to introduce an artificial hydrogen concentration gradient. Concentration profiles on a nm-scale and changes in these due to diffusion at experimental temperatures were measured using NRRA. Taking advantage of the non-destructive nature of NRRA allowed us to observe the evolution of diffusion profiles with time within one sample, and thereby resolve small differences in concentration profile shapes before and after diffusion. Diffusivities are constant over time and show no concentration dependence. The diffusion-temperature relationship is described by an Arrhenius law $D_H = 5.47\ (\pm 13.98) \cdot 10^{-8}\ m^2/s \cdot \exp[-115.6\ (\pm 11.5)\ kJ/mol/RT]$.
2. A determination of diffusion coefficients for hydrogen in NAMs was possible only at high temperatures (>600°C) up to now. However, re-equilibration at shallow depths far from the mantle source would occur at lower temperatures. It was therefore crucial to experimentally verify whether diffusion rates from high temperatures follow an Arrhenius relation to lower temperatures. Our experimental results from experiments

between 195°C and 400°C prove that diffusion coefficients of hydrogen in clinopyroxene can be extrapolated to low temperatures.

3. Non-isothermal diffusion modeling using the newly obtained diffusion coefficients at low temperatures provides information on the degree of re-equilibration as a function of crystal size and cooling rate for a specific P-T-fO_2-path. We modeled the ascent of clinopyroxene (0.5, 1.0, and 2.0 mm) in a temperature range of 600°C–100°C while the concentration at the boundaries are determined by the solubility of hydrogen in clinopyroxene coexisting with a C-saturated C-O-H fluid at the respective P-T-fO_2 conditions. Small clinopyroxene crystals of 0.5 mm preserve original water contents at cooling rates >1,000–10,000°C/yr ($1{\cdot}10^{-3}$–$1{\cdot}10^{-2}$ m/s). However, at slow cooling rates (<10°C/yr) hydrogen contents in even large crystals of 2.0 mm size get substantially modified, thus erasing the hydrogen content equilibrated at mantle depths.

Appendix A: Development of a Non-Isothermal Diffusion Model With Variable System Boundaries

We modeled diffusion of hydrogen in clinopyroxene of different sizes during their ascent along P-T trajectories that are described by two geotherms (oceanic and continental) in a low temperature range of 600°C–100°C in the presence of a C-O-H fluid that is carbon saturated. A calculation of OH concentration profiles that result from these scenarios required a derivation of parameters that affect diffusion, which is outlined in the following. A temperature-depth relationship was derived after Sclater et al. (1980), Equations A1–A3 and Table A1. The quantities in Equations A1–A3 are explained in the table caption.

$$\mathrm{RHP} = \frac{q_{\mathrm{surface}} - q_{\mathrm{base}}}{h_r} \tag{A1}$$

$$T_{\mathrm{crust}} = T_0 + \frac{q_{\mathrm{base}} z}{k_1} + \frac{(q_{\mathrm{surface}} - q_{\mathrm{base}}) \times h_r}{k_1} \left(1 - \mathrm{e}^{-\frac{z}{h_r}}\right) \tag{A2}$$

$$T_{\mathrm{mantle}} = T_{\mathrm{crust\_base}} + \frac{(z - z_{\mathrm{crust}})}{k_2} \times q_{\mathrm{base}} \tag{A3}$$

Table A1
Parameters That Were Used to Compute Geotherms Associated With an Oceanic (OC) and a Continental (CT) Setting

	Crust						Mantle		
Setting	d_c (km)	ρ_c (kg/m³)	q_{surface} (mW/m²)	RHP (μW/cm³)	k_c (W/K m)	h_r (km)	ρ_m (kg/m³)	q_{base} (mW/m²)	k_m (W/K m)
OC	10[1]	2900[2]	34[4]	0.89	2.51[4]	10	3380[5]	25.1[4]	3.35[4]
CT	40[1]	2830[3]	46[4]	1.20	2.51[4]	10	3380[5]	34.0[4]	3.35[4]

Note. d_c = Thickness of the Crust, ρ_c = Density of the Crust, q_{surface} = Surface Heat Flow, RHP = Radiogenic Heat production, k_c: thermal Conductivity of the Crust, h_r = Ratio of Heat Flow to Heat Production, ρ_m = Density of the Mantle, q_{base} = Heat Flow base of Crust, k_m = Thermal Conductivity Mantle. 1 = Philpotts and Ague (2009), 2 = Carlson and Herrick (1990), 3 = Christensen and Mooney (1995), 4 = Sclater et al. (1980), 5 = Dziewonski and Anderson (1981).

The lithostatic pressure along the geotherms was calculated by integrating the densities with depth followed by multiplication with the constant for acceleration due to gravity. The oxygen fugacity was assumed to be continuously buffered by a QMF assemblage. Whether hydration or dehydration occurs also depends on the solubility of hydroxyl in clinopyroxene at respective conditions and the availability of a hydrogen source (in this case a fluid). The solubility of hydrogen in NAM is a function of pressure, temperature, and fH_2O, but is also affected by contents of certain elements (e.g., Al) and fO_2 (Liu & Yang, 2020). We used the solubility law, Equation A4, and experimentally determined values by Liu and Yang (2020) and Bromiley et al. (2004) (dH = 21.2 kJ/mol, dV = 7.3 cm³/mol, A = 7.144 ppm/bar, n = 0.5) to describe solubility of hydroxyl (c_{water} in wt. ppm H_2O) in clinopyroxene as a function of temperature, pressure, and H_2O fugacity (fH_2O). The latter is controlled by the speciation of the present fluid, which was determined from thermodynamic modeling of a C-O-H (carbon saturated and fixed fO_2 at QMF) fluid as a function of temperature, pressure, and fO_2 following the procedure in

Huizenga (2005). The database of fugacity coefficients of the species used in Huizenga (2005) had to be extended by extrapolation in P-T space (between 100°C and 300°C), which is a sufficient approximation for our purpose. OH contents that were derived from the solubility law were used as boundary concentrations that were constantly changing (i.e., decreasing) and thereby introducing a concentration gradient at the system boundaries.

$$c_{\text{water}} = A f\mathrm{H_2O}^{n} \exp\left(-\frac{\mathrm{d}H^{1\text{bar}} + \mathrm{d}V^{\text{solid}} P}{RT}\right) \tag{A4}$$

In the final model, the rate of diffusion is affected by changes in temperature and was thus computed as non-isothermal process by allowing the diffusion coefficient to change according to the respective temperature. The diffusion coefficients were derived through the Arrhenius relationship $D_H = 5.47(\pm 13.98) \cdot 10^{-8}$ m^2/s $\cdot \exp$ [−115.6 (±11.5) kJ/mol/RT] which was obtained through our experiments. Effects of pressure and fO_2 on hydrogen diffusion in clinopyroxene are experimentally weakly or not constrained. The actual diffusion modeling was performed by approximating Fick's second law (Equation A5) by an explicit numerical solution (finite difference, Equation A6).

$$\frac{\partial c(x,t)}{\partial t} = D\frac{\partial^2 c(x,t)}{\partial x^2} \tag{A5}$$

$$c_{i,j+1} = c_{i,j} + \frac{D \cdot \Delta t}{\Delta x^2} \cdot \left[c_{i+1,j} - 2c_{i,j} + c_{i-1,j}\right] \tag{A6}$$

The initial condition ($t = 0$) for the diffusion model is a homogeneous hydrogen distribution in the crystal. This initial concentration corresponds to the solubility of OH in clinopyroxene at the starting P-T-$f\mathrm{H_2O}$ condition. During the diffusion calculation the diffusion rate D_H is continuously changed according to the temperature at that time step. All codes that were used in these calculations are provided in Supporting Information S1.

Appendix B: Fitting Re-Equilibration as a Function of Crystal Size and Cooling Rate

Re-equilibration is defined by Equation B1 with c_{initial} being the initial OH concentration ($t = 0$), $c_{\text{model core}}$ being the OH concentration in the crystal core after diffusion, $c_{\text{equilibrium at } T(\text{final})}$ being the equilibrium concentration at the final temperature (here 100°C). The degree of re-equilibration is calculated for each crystal size, cooling rate, and geotherm. The re-equilibration—cooling rate relationship (Figures S1 and S2 in Supporting Information S1) is then fitted using Equation B2 to obtain parameters $p1$, $q1$, $q2$ for each geotherm and crystal size (Table B1). *MATLAB curve fitting* tool and the implemented non-linear least square procedure (Levenberg-Marquardt algorithm) was used for all fitting procedures that are described in this chapter.

$$\text{re} - \text{equilibration}\,(\%) = \frac{c_{\text{initial}} - c_{\text{model core}}}{c_{\text{initial}} - c_{\text{equilibrium at } T(\text{final})}} \times 100 \tag{B1}$$

$$\text{re} - \text{equilibration}\,(\%) = \frac{p1}{cr^2 + q1 \times cr + q2} \tag{B2}$$

Table B1
Parameters p1, q1, q2 Obtained by Fitting Re-Equilibration—Cooling Rate Relationships for Each Crystal Size and Geotherm

Geotherm/crystal size	$p1$	$q1$	$q2$	R^2
CT/0.5 mm	$9.972{\cdot}10^6$	$1.955{\cdot}10^3$	$1.118{\cdot}10^5$	0.9826
CT/1.0 mm	$9.492{\cdot}10^5$	$7.668{\cdot}10^2$	$1.081{\cdot}10^4$	0.9955
CT/2.0 mm	$8.962{\cdot}10^4$	$2.665{\cdot}10^2$	$1.060{\cdot}10^3$	0.9958
OC/0.5 mm	$1.889{\cdot}10^{10}$	$1.307{\cdot}10^7$	$2.067{\cdot}10^8$	0.9668
OC/1.0 mm	$4.902{\cdot}10^5$	$9.293{\cdot}10^2$	$6.008{\cdot}10^3$	0.9899
OC/2.0 mm	$9.555{\cdot}10^4$	$7.263{\cdot}10^2$	$1.220{\cdot}10^3$	0.9990

The fitting parameters *p1*, *q1*, and *q2* were then fitted as a function of crystal size for both geotherms using simple power-law equations (Equations B3–B5, Table B2).

$$p1 = p1a \times sz^{p1b} \tag{B3}$$

$$q1 = q1a \times sz^{q1b} \tag{B4}$$

$$q2 = q2a \times sz^{q2b} \tag{B5}$$

Table B2
Parameters Obtained by Fitting Re-Equilibration as a Function of Crystal Size (sz) and Cooling Rate (Cr) for the Two Geotherms CT and OC

Parameter	CT	OC
p1a	$9.4663 \cdot 10^5$	$9.6171 \cdot 10^6$
p1b	−3.399	−8.8003
R^2	1.00	1.00
q1a	$7.3650 \cdot 10^2$	$2.0662 \cdot 10^4$
q1b	−1.4375	−7.0677
R^2	0.99	1.00
q2a	$1.0861 \cdot 10^4$	$1.1485 \cdot 10^5$
q2b	−3.3604	−8.6851
R^2	1.00	1.00

Substituting parameters *p1*, *q1*, and *q2* in Equation B2 by the power-law Equations B3–B5 above yields the following Equation B6 that was used to calculate re-equilibration in % as a function of crystal size *sz* in mm and cooling rate *cr* in °C/yr for both geotherms.

$$\text{re} - \text{equilibration}\,(\%) = \frac{p1a \times sz^{p1b}}{cr^2 + q1a \times sz^{q1b} \times cr + q2a \times sz^{q2b}} \tag{B6}$$

Data Availability Statement

The entire data set, all MATLAB© programs that were used in this study, and instructions on how to use the data are given in Supporting Information S1. All data is accessible and can be downloaded from https://doi.org/10.5281/zenodo.7290350.

Acknowledgments
T. Bissbort thanks J. Primocerio for providing the EPMA data of clinopyroxene used in this study and C. Hirschle for Laue analysis for crystal orientation. He also thanks C. Beyer for his assistance in the lab. T. Bissbort expresses great gratitude for the operators and technical staff at the Dynamitron-Tandem-Laboratorium (RUBION). This work greatly benefited from the thoughtful reviews by J. Hermann and one anonymous reviewer. This research is funded by the DFG Project nos. BE 1307/5-1 and CH 166/20-1. Open Access funding enabled and organized by Projekt DEAL.

References

Becker, H. W., Bahr, M., Berheide, M., Borucki, L., Buschmann, M., Rolfs, C., et al. (1995). Hydrogen depth profiling using ^{18}O ions. *Zeitschrift für Physik A Hadrons and nuclei*, *351*(4), 453–465. https://doi.org/10.1007/BF01291151

Becker, H.-W., & Rogalla, D. (2016). Nuclear reaction analysis. In H. Fritzsche, J. Huot, & D. Fruchart (Eds.), *Neutron scattering and other nuclear techniques for hydrogen in materials* (pp. 315–336). Springer (Neutron scattering applications and techniques).

Bell, D. R., & Rossman, G. R. (1992). Water in Earth's mantle: The role of nominally anhydrous minerals. *Science*, *255*(5050), 1391–1397. https://doi.org/10.1126/science.255.5050.1391

Beran, A., & Zemann, J. (1969). Über OH-Gruppen in Olivin. *Oesterr Akad Wiss math Naturwiss Kl Anzeiger*, *73*, 74.

Bissbort, T., Becker, H.-W., Fanara, S., & Chakraborty, S. (2021). Novel approach to study diffusion of hydrogen bearing species in silicate glasses at low temperatures. *Chemical Geology*, *562*, 120037. https://doi.org/10.1016/j.chemgeo.2020.120037

Bromiley, G. D., Keppler, H., McCammon, C., Bromiley, F. A., & Jacobsen, S. D. (2004). Hydrogen solubility and speciation in natural, gem-quality chromian diopside. *American Mineralogist*, *89*(7), 941–949. https://doi.org/10.2138/am-2004-0703

Carlson, R. L., & Herrick, C. N. (1990). Densities and porosities in the oceanic crust and their variations with depth and age. *Journal of Geophysical Research*, *95*(B6), 9153. https://doi.org/10.1029/JB095iB06p09153

Chakraborty, S., & Ganguly, J. (1991). Compositional zoning and cation diffusion in garnets. In *Diffusion, atomic ordering, and mass transport* (pp. 20–175). Springer. Retrieved from https://link.springer.com/chapter/10.1007/978-1-4613-9019-0_4

Chen, S., Hiraga, T., & Kohlstedt, D. L. (2006). Water weakening of clinopyroxene in the dislocation creep regime. *Journal of Geophysical Research*, *111*, B8. https://doi.org/10.1029/2005JB003885

Christensen, N. I., & Mooney, W. D. (1995). Seismic velocity structure and composition of the continental crust: A global view. *Journal of Geophysical Research*, *100*(B6), 9761–9788. https://doi.org/10.1029/95JB00259

Costa, F., Chakraborty, S., & Dohmen, R. (2003). Diffusion coupling between trace and major elements and a model for calculation of magma residence times using plagioclase. *Geochimica et Cosmochimica Acta*, *67*(12), 2189–2200. https://doi.org/10.1016/S0016-7037(02)01345-5

Costa, F., Dohmen, R., & Chakraborty, S. (2008). Time scales of magmatic processes from modeling the zoning patterns of crystals. *Reviews in Mineralogy and Geochemistry*, *69*(1), 545–594. https://doi.org/10.2138/rmg.2008.69.14

Demers-Roberge, A., Jollands, M. C., Tollan, P., & Müntener, O. (2021). H diffusion in orthopyroxene and the retention of mantle water signatures. *Geochimica et Cosmochimica Acta*, *305*, 263–281. https://doi.org/10.1016/j.gca.2021.04.005

Demouchy, S., Jacobsen, S. D., Gaillard, F., & Stern, C. R. (2006). Rapid magma ascent recorded by water diffusion profiles in mantle olivine. *Geology*, *34*(6), 429. https://doi.org/10.1130/G22386.1

Demouchy, S., & Mackwell, S. (2006). Mechanisms of hydrogen incorporation and diffusion in iron-bearing olivine. *Physics and Chemistry of Minerals*, *33*(5), 347–355. https://doi.org/10.1007/s00269-006-0081-2

Demouchy, S., Thoraval, C., Bolfan-Casanova, N., & Manthilake, G. (2016). Diffusivity of hydrogen in iron-bearing olivine at 3GPa. *Physics of the Earth and Planetary Interiors*, *260*, 1–13. https://doi.org/10.1016/j.pepi.2016.08.005

Droop, G. T. R. (1987). A general equation for estimating Fe^{3+} concentrations in ferromagnesian silicates and oxides from microprobe analyses, using stoichiometric criteria. *Mineralogical Magazine*, *51*(361), 431–435. https://doi.org/10.1180/minmag.1987.051.361.10

Dziewonski, A. M., & Anderson, D. L. (1981). Preliminary reference Earth model. *Physics of the Earth and Planetary Interiors*, *25*(4), 297–356. https://doi.org/10.1016/0031-9201(81)90046-7

Faak, K., Chakraborty, S., & Coogan, L. A. (2013). Mg in plagioclase. Experimental calibration of a new geothermometer and diffusion coefficients. *Geochimica et Cosmochimica Acta*, *123*, 195–217. https://doi.org/10.1016/j.gca.2013.05.009

Fei, H., Druzhbin, D., & Katsura, T. (2020). The effect of water on ionic conductivity in olivine. *Journal of Geophysical Research: Solid Earth*, *125*, 3. https://doi.org/10.1029/2019JB019313

Ferriss, E., Plank, T., Newcombe, M., Walker, D., & Hauri, E. (2018). Rates of dehydration of olivines from San Carlos and Kilauea Iki. *Geochimica et Cosmochimica Acta*, *242*, 165–190. https://doi.org/10.1016/j.gca.2018.08.050

Ferriss, E., Plank, T., & Walker, D. (2016). Site-specific hydrogen diffusion rates during clinopyroxene dehydration. *Contributions to Mineralogy and Petrology*, *171*(6), 55. https://doi.org/10.1007/s00410-016-1262-8

Gose, J., Schmädicke, E., & Stalder, R. (2011). Water in mantle orthopyroxene—No visible change in defect water during serpentinization. *European Journal of Mineralogy*, *23*(4), 529–536. https://doi.org/10.1127/0935-1221/2011/0023-2122

Guillot, S., Schwartz, S., Reynard, B., Agard, P., & Prigent, C. (2015). Tectonic significance of serpentinites. *Tectonophysics*, *646*, 1–19. https://doi.org/10.1016/j.tecto.2015.01.020

Hercule, S., & Ingrin, J. (1999). Hydrogen in diopside; diffusion, kinetics of extraction-incorporation, and solubility. *American Mineralogist*, *84*(10), 1577–1587. https://doi.org/10.2138/am-1999-1011

Hirschmann, M. (2006). Water, melting, and the deep Earth H_2O cycle. *Annual Review of Earth and Planetary Sciences*, *34*(1), 629–653. https://doi.org/10.1146/annurev.earth.34.031405.125211

Hirschmann, M., & Kohlstedt, D. L. (2012). Water in Earth's mantle. *Physics Today*, *65*(3), 40–45. https://doi.org/10.1063/pt.3.1476

Hirth, G., & Kohlstedt, D. L. (1996). Water in the oceanic upper mantle: Implications for rheology, melt extraction and the evolution of the lithosphere. *Earth and Planetary Science Letters*, *144*(1–2), 93–108. https://doi.org/10.1016/0012-821X(96)00154-9

Huizenga, J. M. (2005). COH, an Excel spreadsheet for composition calculations in the C–O–H fluid system. *Computers & Geosciences*, *31*(6), 797–800. https://doi.org/10.1016/j.cageo.2005.03.003

Ingrin, J., Hercule, S., & Charton, T. (1995). Diffusion of hydrogen in diopside: Results of dehydration experiments. *Journal of Geophysical Research*, *100*(B8), 15489–15499. https://doi.org/10.1029/95JB00754

Jollands, M. C., Ellis, B., Tollan, P. M. E., & Müntener, O. (2020). An eruption chronometer based on experimentally determined H-Li and H-Na diffusion in quartz applied to the Bishop Tuff. *Earth and Planetary Science Letters*, *551*, 116560. https://doi.org/10.1016/j.epsl.2020.116560

Jollands, M. C., O'Neill, H. S. C., Berry, A. J., Le Losq, C., Rivard, C., & Hermann, J. (2021). A combined Fourier transform infrared and Cr K-edge X-ray absorption near-edge structure spectroscopy study of the substitution and diffusion of H in Cr-doped forsterite. *European Journal of Mineralogy*, *33*(1), 113–138. https://doi.org/10.5194/ejm-33-113-2021

Karato, S. (1990). The role of hydrogen in the electrical conductivity of the upper mantle. *Nature*, *347*(6290), 272–273. https://doi.org/10.1038/347272a0

Karato, S., & Jung, H. (1998). Water, partial melting and the origin of the seismic low velocity and high attenuation zone in the upper mantle. *Earth and Planetary Science Letters*, *157*(3–4), 193–207. https://doi.org/10.1016/S0012-821X(98)00034-X

Katayama, I., Nakashima, S., & Yurimoto, H. (2006). Water content in natural eclogite and implication for water transport into the deep upper mantle. *Lithos*, *86*(3–4), 245–259. https://doi.org/10.1016/j.lithos.2005.06.006

Keppler, H., & Bolfan-Casanova, N. (2006). Thermodynamics of water solubility and partitioning. *Reviews in Mineralogy and Geochemistry*, *62*(1), 193–230. https://doi.org/10.2138/rmg.2006.62.9

Keppler, H., & Smyth, J. R. (2006). *Water in nominally anhydrous minerals* (Vol. 62). De Gruyter (Reviews in Mineralogy & Geochemistry).

Kilgore, M. L., Peslier, A. H., Brandon, A. D., Schaffer, L. A., Morris, R. V., Graff, T. G., et al. (2020). Metasomatic control of hydrogen contents in the layered cratonic mantle lithosphere sampled by Lac de Gras xenoliths in the central Slave craton, Canada. *Geochimica et Cosmochimica Acta*, *286*, 29–53. https://doi.org/10.1016/j.gca.2020.07.013

Kohlstedt, D. L., Keppler, H., & Rubie, D. C. (1996). Solubility of water in the α, β and γ phases of $(Mg, Fe)_2SiO_4$. *Contributions to Mineralogy and Petrology*, *123*(4), 345–357. https://doi.org/10.1007/s004100050161

Konzett, J., Libowitzky, E., Hejny, C., Miller, C., & Zanetti, A. (2008). Oriented quartz+calcic amphibole inclusions in omphacite from the Saualpe and Pohorje mountain eclogites, eastern Alps—An assessment of possible formation mechanisms based on IR- and mineral chemical data and water storage in eastern Alpine eclogites. *Lithos*, *106*(3–4), 336–350. https://doi.org/10.1016/j.lithos.2008.09.002

Kumamoto, K. M., Warren, J. M., & Hauri, E. H. (2019). Evolution of the Josephine peridotite shear zones: 1. Compositional variation and shear initiation. *Geochemistry, Geophysics, Geosystems*, *20*(12), 5765–5785. https://doi.org/10.1029/2019GC008399

Le Roux, V., Urann, B. M., Brunelli, D., Bonatti, E., Cipriani, A., Demouchy, S., & Monteleone, B. D. (2021). Postmelting hydrogen enrichment in the oceanic lithosphere. *Science Advances*, *7*(24), eabf6071. https://doi.org/10.1126/sciadv.abf6071

Liu, H., & Yang, X. (2020). Solubility of hydroxyl groups in pyroxenes: Effect of oxygen fugacity at 0.2–3 GPa and 800–1200°C. *Geochimica et Cosmochimica Acta*, *286*, 355–379. https://doi.org/10.1016/J.GCA.2020.07.034

Lynn, K. J., Shea, T., & Garcia, M. O. (2017). Nickel variability in Hawaiian olivine: Evaluating the relative contributions from mantle and crustal processes. *American Mineralogist*, *102*(3), 507–518. https://doi.org/10.2138/am-2017-5763

Lynn, K. J., & Warren, J. M. (2021). The potential for aqueous fluid-rock and silicate melt-rock interactions to re-equilibrate hydrogen in peridotite nominally anhydrous minerals. *American Mineralogist*, *106*(5), 701–714. https://doi.org/10.2138/am-2021-7435

Mackwell, S. J., & Kohlstedt, D. L. (1990). Diffusion of hydrogen in olivine: Implications for water in the mantle. *Journal of Geophysical Research*, *95*(B4), 5079. https://doi.org/10.1029/JB095iB04p05079

Maurel, B., & Amsel, G. (1983). A new measurement of the 429 keV 15N(p, ay)12C resonance. Applications of the very narrow width found to 15N and 1H depth location. *Nuclear Instruments and Methods in Physics Research*, *218*(1–3), 159–164. https://doi.org/10.1016/0167-5087(83)90973-0

Moine, B. N., Bolfan-Casanova, N., Radu, I. B., Ionov, D. A., Costin, G., Korsakov, A. V., et al. (2020). Molecular hydrogen in minerals as a clue to interpret ∂D variations in the mantle. *Nature Communications*, *11*(1), 3604. https://doi.org/10.1038/s41467-020-17442-8

Müller, T., Dohmen, R., Becker, H. W., ter Heege, J. H., & Chakraborty, S. (2013). Fe–Mg interdiffusion rates in clinopyroxene: Experimental data and implications for Fe–Mg exchange geothermometers. *Contributions to Mineralogy and Petrology*, *166*(6), 1563–1576. https://doi.org/10.1007/s00410-013-0941-y

Newcombe, M. E., Plank, T., Barth, A., Asimow, P. D., & Hauri, E. (2020). Water-in-olivine magma ascent chronometry: Every crystal is a clock. *Journal of Volcanology and Geothermal Research*, *398*, 106872. https://doi.org/10.1016/j.jvolgeores.2020.106872

Ohtani, E., & Litasov, K. D. (2006). The effect of water on mantle phase transitions. *Reviews in Mineralogy and Geochemistry*, *62*(1), 397–420. https://doi.org/10.2138/rmg.2006.62.17

Osipowicz, T., Lieb, K. P., & Brüssermann, S. (1987). Nuclear instruments and methods.

Padrón-Navarta, J. A., Hermann, J., & St. O'Neill, H. C. (2014). Site-specific hydrogen diffusion rates in forsterite. *Earth and Planetary Science Letters*, *392*, 100–112. https://doi.org/10.1016/j.epsl.2014.01.055

Peslier, A. H., & Bizimis, M. (2015). Water in Hawaiian peridotite minerals: A case for a dry metasomatized oceanic mantle lithosphere. *Geochemistry, Geophysics, Geosystems*, *16*(4), 1211–1232. https://doi.org/10.1002/2015GC005780

Peslier, A. H., Bizimis, M., & Matney, M. (2015). Water disequilibrium in olivines from Hawaiian peridotites: Recent metasomatism, H diffusion and magma ascent rates. *Geochimica et Cosmochimica Acta*, *154*, 98–117. https://doi.org/10.1016/j.gca.2015.01.030

Peslier, A. H., Woodland, A. B., & Wolff, J. A. (2008). Fast kimberlite ascent rates estimated from hydrogen diffusion profiles in xenolithic mantle olivines from southern Africa. *Geochimica et Cosmochimica Acta*, *72*(11), 2711–2722. https://doi.org/10.1016/j.gca.2008.03.019

Philpotts, A., & Ague, J. (2009). *Principles of igneous and metamorphic petrology*. Cambridge University Press.

Reynes, J., Jollands, M., Hermann, J., & Ireland, T. (2018). Experimental constraints on hydrogen diffusion in garnet. *Contributions to Mineralogy and Petrology*, *173*, 9. https://doi.org/10.1007/s00410-018-1492-z

Rossman, G. R. (1996). Studies of OH in nominally anhydrous minerals. *Physics and Chemistry of Minerals*, *23*(4–5), 4–5. https://doi.org/10.1007/BF00207777

Schaible, M. J., & Baragiola, R. A. (2014). Hydrogen implantation in silicates: The role of solar wind in SiOH bond formation on the surfaces of airless bodies in space. *Journal of Geophysical Research: Planets*, *119*(9), 2017–2028. https://doi.org/10.1002/2014JE004650

Sclater, J. G., Jaupart, C., & Galson, D. (1980). The heat flow through oceanic and continental crust and the heat loss of the Earth. *Reviews of Geophysics*, *18*(1), 269. https://doi.org/10.1029/RG018i001p00269

Skogby, H. (1994). OH incorporation in synthetic clinopyroxene. *American Mineralogist*, *79*(3–4), 240–249.

Skogby, H., Bell, D. R., & Rossman, G. R. (1990). Hydroxide in pyroxene; variations in the natural environment. *American Mineralogist*, *75*(7–8), 764–774.

Skogby, H., & Rossman, G. R. (1989). OH- in pyroxene; an experimental study of incorporation mechanisms and stability. *American Mineralogist*, *74*(9–10), 1059–1069.

Smyth, J. R., Bell, D. R., & Rossman, G. R. (1991). Incorporation of hydroxyl in upper-mantle clinopyroxenes. *Nature*, *351*(6329), 732–735. https://doi.org/10.1038/351732a0

Stalder, R., & Behrens, H. (2006). D/H exchange in pure and Cr-doped enstatite: Implications for hydrogen diffusivity. *Physics and Chemistry of Minerals*, *33*(8–9), 601–611. https://doi.org/10.1007/s00269-006-0112-z

Stalder, R., & Skogby, H. (2003). Hydrogen diffusion in natural and synthetic orthopyroxene. *Physics and Chemistry of Minerals*, *30*(1), 12–19. https://doi.org/10.1007/s00269-002-0285-z

Sundvall, R., Skogby, H., & Stalder, R. (2009). Hydrogen diffusion in synthetic Fe-free diopside. *European Journal of Mineralogy*, *21*(5), 963–970. https://doi.org/10.1127/0935-1221/2009/0021-1971

Tang, W., Hui, H., Ionov, D. A., Chen, W., Zhang, L., & Xu, Y. (2020). Metasomatism-controlled hydrogen distribution in the Spitsbergen upper mantle. *American Mineralogist*, *105*(9), 1326–1341. https://doi.org/10.2138/am-2020-7290

Thoraval, C., Demouchy, S., & Padrón-Navarta, J. A. (2019). Relative diffusivities of hydrous defects from a partially dehydrated natural olivine. *Physics and Chemistry of Minerals*, *46*(1), 1–13. https://doi.org/10.1007/s00269-018-0982-x

Tollan, P. M. E., Smith, R., O'Neill, H. S. C., & Hermann, J. (2017). The responses of the four main substitution mechanisms of H in olivine to H_2O activity at 1050°C and 3 GPa. *Progress in Earth and Planetary Science*, *4*, 1. https://doi.org/10.1186/s40645-017-0128-7

Traeger, F., Kauer, M., Wöll, C., Rogalla, D., & Becker, H.-W. (2011). Analysis of surface, subsurface, and bulk hydrogen in ZnO using nuclear reaction analysis. *Physical Review B: Condensed Matter*, *84*(7), 33. https://doi.org/10.1103/PhysRevB.84.075462

Urann, B. M., Le Roux, V., Jagoutz, O., Müntener, O., Behn, M. D., & Chin, E. J. (2022). High water content of arc magmas recorded in cumulates from subduction zone lower crust. *Nature Geoscience*, *15*(6), 501–508. https://doi.org/10.1038/s41561-022-00947-wa

Wang, Y.-F., Qin, J.-Y., Soustelle, V., Zhang, J.-F., & Xu, H.-J. (2021). Pyroxene does not always preserve its source hydrogen concentration: Clues from some peridotite xenoliths. *Geochimica et Cosmochimica Acta*, *292*, 382–408. https://doi.org/10.1016/j.gca.2020.10.003

Warren, J. M., & Hauri, E. H. (2014). Pyroxenes as tracers of mantle water variations. *Journal of Geophysical Research: Solid Earth*, *119*(3), 1851–1881. https://doi.org/10.1002/2013JB010328

Woods, S. C., Mackwell, S., & Dyar, D. (2000). Hydrogen in diopside. Diffusion profiles. *American Mineralogist*, *85*(3–4), 480–487. https://doi.org/10.2138/am-2000-0409

Zhang, Y., Bae, I.-T., Sun, K., Wang, C., Ishimaru, M., Zhu, Z., et al. (2009). Damage profile and ion distribution of slow heavy ions in compounds. *Journal of Applied Physics*, *105*(10), 104901. https://doi.org/10.1063/1.3118582

Ziegler, J. F., Ziegler, M. D., & Biersack, J. P. (2010). SRIM – The stopping and range of ions in matter (2010). *Nuclear Instruments and Methods in Physics Research Section B: Beam Interactions with Materials and Atoms*, *268*(11–12), 1818–1823. https://doi.org/10.1016/j.nimb.2010.02.091

References From the Supporting Information

Shi, P., & Saxena, S. K. (1992). Thermodynamic modeling of the C-H-O-S fluid system. *American Mineralogist*, *77*, 1038–1049.